

Observation of Weak Counterion Size Dependence of Thermoelectric Transport in Ion Exchange Doped Conducting Polymers Across a Wide Range of Conductivities


Chen Chen, Ian E. Jacobs,* Keehoon Kang, Yue Lin, Cameron Jellett, Boseok Kang, Seon Baek Lee, Yuxuan Huang, Mohammad Balooch Qarai, Raja Ghosh, Martin Statz, William Wood, Xinglong Ren, Dion Tjhe, Yuanhui Sun, Xiaojian She, Yuanyuan Hu, Lang Jiang, Frank C. Spano, Iain McCulloch, and Henning Sirringhaus*

Conducting polymers are of interest for a broad range of applications from bioelectronics to thermoelectrics. The factors that govern their complex charge transport physics include the structural disorder present in these highly doped polymer films and the Coulombic interactions between the electronic charge carriers and the dopant counterions. Previous studies have shown that at low doping levels carriers are strongly trapped in the vicinity of the counterions, while at high doping levels charge transport is not limited by Coulombic trapping, which manifests itself in the conductivity being independent of the size of the dopant counterion. Here a recently developed ion exchange doping method is used to investigate the ion size dependence of a semicrystalline polythiophene-based model system across a wide range of conductivities. It is found that the regime in which the charge and thermoelectric transport is not or only weakly dependent on ion size, extends to surprisingly low conductivities. This surprising observation is explained by a heterogeneous doping that involves doping of the amorphous domains to high doping levels first before doping of the ordered, crystalline domains occurs. The study provides new insights into how the thermoelectric physics of conducting polymers evolves as a function of doping level.

1. Introduction

Polymer-based organic thermoelectric materials (OTEs) show great promise for the development of flexible thermoelectric and wearable/portable smart devices with energy harvesting, thermoregulation, and temperature sensing capabilities^[1] due to their intrinsic merits of low cost, light weight, mechanical robustness and flexibility, ease of synthesis, tailoring of material properties and environmental friendliness.^[2] Hence, the last decade has witnessed intense efforts devoted to pushing up the thermoelectric (TE) performances of OTEs and power factors (PF) to $2710 \mu\text{W m}^{-1} \text{K}^{-2}$ ^[3] and figure of merit (ZT) of ≈ 0.5 .^[4] However, such exceptional thermoelectric performance still lags behind inorganic materials, such as SnSe single crystals with a record ZT of ≈ 2.7 ,^[5] and have been achieved primarily in Poly(3,4-ethylenedioxythiophene)

C. Chen,^[†] I. E. Jacobs, Y. Lin, Y. Huang, M. Statz, W. Wood, X. Ren, D. Tjhe, Y. Sun, H. Sirringhaus
Optoelectronics Group
Cavendish Laboratory
University of Cambridge
J Thomson Avenue, Cambridge CB3 0HE, UK
E-mail: ij255@cam.ac.uk; hs220@cam.ac.uk

 The ORCID identification number(s) for the author(s) of this article can be found under <https://doi.org/10.1002/aenm.202202797>.

© 2023 The Authors. Advanced Energy Materials published by Wiley-VCH GmbH. This is an open access article under the terms of the Creative Commons Attribution License, which permits use, distribution and reproduction in any medium, provided the original work is properly cited.

^[†]Present address: Science and Technology on Advanced Ceramic Fibers & Composites Laboratory, College of Aerospace Science and Engineering, National University of Defense Technology, Changsha 410073, P. R. China

DOI: 10.1002/aenm.202202797

K. Kang
Department of Materials Science and Engineering
Research Institute of Advanced Materials
Seoul National University
Seoul 08826, Korea

C. Jellett, I. McCulloch,
Department of Chemistry
Imperial College London, South Kensington
London SW7 2AZ, UK

B. Kang, S. B. Lee
Department of Chemical Engineering
Pohang University of Science and Technology
Pohang 790-784, Republic of Korea

B. Kang
SKKU Advanced Institute of Nanotechnology and Department
of Nano Engineering
Sungkyunkwan University
Suwon 16419, Republic of Korea

M. Balooch Qarai, R. Ghosh, F. C. Spano
Department of Chemistry
Temple University
Philadelphia, PA 19122, USA

(PEDOT)-based systems.^[3,4,6] In organic systems, the lack of thorough understanding of charge and entropy transport mechanisms as well as structure–property relationships impede the development of molecular design guidelines for the optimization of TE performance.^[7]

Conducting polymers are doped to improve the conductivity (σ),^[8] which is particularly important for improving their power factor $PF = S^2 \sigma$ and figure of merit $ZT = \frac{S^2 \sigma}{\kappa} T$, where κ is the thermal conductivity. The Seebeck coefficient S tends to decrease when carrier concentration and conductivity increase.^[9] Therefore, it is crucial to find an optimum doping level at which the PF is maximized. Many doped polymers, except some PEDOT-based systems,^[10] have never reached their peak PF s,^[11] but recently developed ion exchange^[12] and electrolyte gating doping methods^[13] allow pushing the doping concentration in conducting polymers to $\approx 10^{21} \text{ cm}^{-3}$ with around one charge per monomer.^[14] At such high doping concentrations, the charge and thermoelectric transport shows distinctively different mechanisms, which could be quasimetallic,^[13,15] semimetallic,^[16] or even show changes in the polarity of the charge carriers^[17] depending on the polymer-dopant systems.

For poly(2,5 bis(3-alkylthiophene-2-yl)thieno[3,2-b]thiophene) (PBTTT) a high PF value of $2000 \mu\text{W m}^{-1} \text{ K}^{-2}$ ^[18] has recently been reported. Although such a high thermoelectric performance has so far not been possible to reproduce,^[19] PBTTT is an interesting model system for understanding thermoelectric transport physics.^[13,15a,18,20] Its performance is comparable to the widely studied PEDOT-based systems,^[3,6] but PBTTT is a semicrystalline solvated polymer with a simpler, single-component microstructure compared to PEDOT and offers the capability of modulating charge carriers in a wide range in an accumulation mode via either electrostatic or electrochemical gating.^[18,21] What makes PBTTT a particularly powerful model system is that it exhibits only relatively minor degradation in crystallinity upon doping. Even at high doping levels approaching the density of repeat unit PBTTT remains highly crystalline when doped with a variety of different ions.^[14b]

At a low charge concentration of 10^{18} – 10^{19} cm^{-3} , the Seebeck coefficient of PBTTT measured in field-effect gated structures,

i.e., without counterions, could be described by a narrow band polaron model in a low disorder limit.^[22] Via conventional molecular doping, the charge density could be increased to $> 10^{20} \text{ cm}^{-3}$ and the emergence of 2D coherent charge transport could be observed,^[23] where S versus σ follows a power law dependence of $\sigma^{-1/4}$.^[23b] Quasimetallic charge transport featuring a partial negative temperature dependence of conductivity, finite conductivity upon extrapolation to 0 Kelvin, Pauli magnetic susceptibility, and negative magnetoconductance has also been observed at even higher doping levels approaching $\approx 10^{21} \text{ cm}^{-3}$.^[12,13,14b,15a] The PF peaks around the onset of such a “metallic” state beyond which the power law relationship between S and σ can be expressed as $S \propto \sigma^{-1}$.^[13,15a]

An important question is whether these transport properties are dependent on the choice and size of the dopant counterion, which determines the electrostatic disorder experienced by the electronic charge carriers on the polymer chains. The ion sizes are usually described by the smallest principal moment of the ionic gyration tensor λ_x , which measures the shortest approach distance to the ionic center of mass and is inversely related to the strength of Coulomb interaction between counterions, as detailed previously.^[14b] Large ions with large λ_x are expected to generate weaker electrostatic disorder than small ions with small λ_x , as the electronic charges tend to be further away from the center of the ions. Because C14-PBTTT (Poly[2,5-bis(3-tetradecylthiophen-2-yl)thieno[3,2-b]thiophene]) retains its crystallinity when dopant ions of different size are incorporated into the interdigitated side chains regions of the polymer microstructure, it is an ideal system to investigate such ion size effects without the need to account for large changes in microstructure when varying the ion size.^[14b] At low doping concentration $< 10^{18}$ – 10^{19} cm^{-3} it is widely accepted that the formation of free carriers and their charge transport is limited by the strong Coulomb interaction between the carriers and the dopant counterions, and therefore that the transport properties should depend strongly on ion size and shape, i.e., on how closely the charge carriers are able to approach the ions.^[24] At high doping levels $> 10^{20} \text{ cm}^{-3}$ on the other hand, recent studies have shown that ion size and counterion-induced Coulomb interactions have a negligible effect on the electrical conductivity^[14b] and mobility,^[25] respectively, as in this regime carriers are sufficiently delocalized to average effectively over the Coulomb potentials generated by the counterions. However, what is currently not well understood is the effect of ion size on the thermoelectric properties in the intermediate doping regime. In particular, it is not clear at which levels of doping and conductivity the regime, in which the transport properties are found to be independent of ion size, sets in.

We can estimate this doping level from the Mott criterion $N_d^{1/3} R_{\text{dop}} \approx 0.2$ where N_d is the dopant density and R_{dop} is the dopant-polaron separation distance. This predicts that at an intermediate doping level $N_d \approx 10^{20} \text{ cm}^{-3}$ for a typical R_{dop} of 0.4 nm, we should start to see the onset of ionic size effects. In C14-PBTTT:TFSI conductivities around 1000 S cm^{-1} can be achieved for the highest doping levels around 10^{21} cm^{-3} . This implies that we might reasonably expect to see the onset of ion size effects around 100 S cm^{-1} , assuming mobility is relatively doping level independent at high carrier density. It is important to investigate whether this is indeed the case. Such an

X. She

State Key Laboratory of Modern Optical Instrumentation
College of Optical Science and Engineering
International Research Center for Advanced Photonics
Zhejiang University
Hangzhou 310000, China

Y. Hu

Key Laboratory for Micro-Nano Optoelectronic Devices
of Ministry of Education
School of Physics and Electronics
Hunan University
Changsha 410082, P. R. China

L. Jiang

Beijing National Laboratory for Molecular Sciences
Institute of Chemistry Chinese Academy of Sciences
Beijing 100190, P. R. China

I. McCulloch

Department of Chemistry
University of Oxford
12 Mansfield Road, Oxford OX1 3TA, UK

intermediate doping regime is generally highly relevant for thermoelectric polymer as it supports higher Seebeck coefficients than what is achievable at the highest doping concentrations.

Herein, we use the recently developed ion exchange doping method^[12,14a] to investigate the thermoelectric properties of C14-PBTTT as a function of size of the counterion across a broad range of doping concentrations/conductivities. We use three chemically homologous, closed-shell anions of different size, tris(trifluoromethylsulfonyl)methide anion (TFSM⁻), the largest anion of the series, bis(trifluoromethylsulfonyl)imide anion (TFSI⁻) of intermediate size as well as trifluoromethanesulfonate (TFO⁻), the smallest anion in the series. We vary their concentrations to achieve conductivities ranging from 10⁻¹ to 10³ S cm⁻¹. We combine spectroscopic characterization by ultraviolet–visible (UV–vis) absorption spectroscopy and Fourier transform infrared spectroscopy (FT-IR), microstructural characterization by grazing incidence wide-angle X-ray scattering (GIWAXS) with measurements of the Seebeck-conductivity (S - σ) relationship and the temperature dependence of Seebeck coefficient (S) and conductivity (σ). We analyze the thermoelectric transport data using the Kang–Snyder model^[11] and aim to understand better the relationship between microstructure, transport mechanism, and the counterion size dependence of thermoelectric performance, with a focus on the intermediate doping regime. We find that the regime in which conductivity is independent of ion size extends far beyond the expected onset around 100 S cm⁻¹ down to conductivities as low as 0.1–1 S cm⁻¹ and we identify the physical mechanism for this surprising observation.

2. Results and Discussion

2.1. Efficient Doping of C14-PBTTT via Ion Exchange

Ion exchange doping has been proven to be a powerful tool to tune the charge concentration of conducting polymers across a broad range up to the degenerate limit and to provide great ease and flexibility in the choice of counterions for investigation of the ion size effects on the transport properties.^[14b,25] Ion exchange doping is closely related to electrochemical doping but does not require the presence of electrodes, making it more suitable for device fabrication. The process involves three stages (see **Figure 1a**): 1) Charge transfer from the polymer (PBTTT) to an oxidizing agent at the interface between the polymer film and the dopant solution, creating a positive polaron. Here we use Fe³⁺ obtained from the disproportionation of FeCl₃ to Fe³⁺ and FeCl₄⁻ in acetonitrile as oxidizing agent. 2) Ion exchange of the dopant anion (FeCl₄⁻) with the anion of an ionic liquid in the dopant solution (in our case TFSM⁻, TFSI⁻, TFO⁻). This process is driven entropically by a large concentration difference between the dopant ions and the ionic liquid anions in the dopant solution. 3) The ionic liquid anion and the positive polaron on the polymer induced in step (1) diffuse into the bulk of the polymer film. Compared to conventional molecular doping, ion exchange doping offers the advantage that requirements for inducing the initial electron transfer and the incorporation of the charge stabilizing counterions can be separated and that the counterion can be selected from a broad range

of stable, closed-shell anions as opposed to a narrow range of unstable radicals. For a detailed discussion of the ion exchange doping method, we refer to the work by Watanabe et al.^[12] and Jacobs et al.^[14a]

To evaluate the extent of doping in PBTTT films by the three ionic liquids selected we performed UV–vis absorption spectroscopy (Figure 1b–d). Experimental details of the device fabrication for these measurements as well as for the thermoelectric characterization discussed below can be found in the Supporting Information Sections 1–3. The UV–vis spectra show similar changes throughout the doping levels for the three systems studied here. The neutral absorption peak of PBTTT centered around 560 nm (2.2 eV) becomes bleached, and the sub-band absorption peak around 860 nm (1.4 eV) due to the P2 polaron band^[26] rises with increasing exposure time and concentration, respectively, of the doping solution. Interestingly, the P2 polaron peak reaches a maximum at some intermediate doping level (e.g., PBTTT-TFSI⁻ and PBTTT-TFSM⁻ prepared with the exposure time of 10 and 20 s, respectively) before decreasing slightly at longer exposure times. Such a decrease in the intensity of the P2 peak as we approach maximum doping could originate either from the bipolaron formation,^[27] a reduction of the oscillator strength of the P2 band reflecting increased charge delocalization,^[28] or perhaps a combination of these two effects.^[29] The question of polaron delocalization will be discussed in more detail in Section 2.6 below.

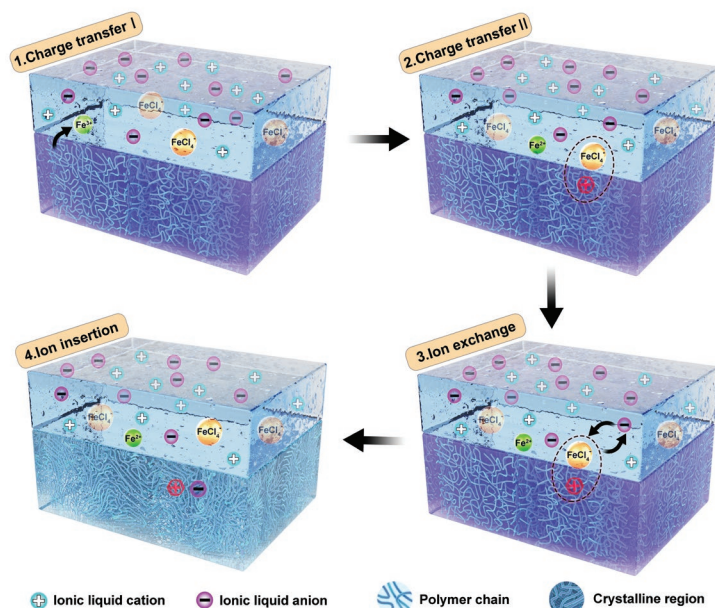
Figure 1e–g shows how the corresponding conductivity for PBTTT-TFO⁻, PBTTT-TFSI⁻, and PBTTT-TFSM⁻ doped films, respectively, evolve with exposure time and doping concentration, respectively. We observe a sharp increase of conductivity as the doping level rises before it reaches a plateau in the high doping region. In all three systems the maximum conductivities ($\approx 10^3$ S cm⁻¹) achieved here approach values for disordered inorganic metals.^[30]

2.2. Microstructural Evolution as a Function of the Anion Size

Doping is expected to introduce a perturbation of the microstructure and could thus affect the charge transport in addition to the effects of counterion-induced Coulomb interactions.^[31] Therefore, it is crucial to monitor the microstructural evolution before and after doping. Here, GIWAXS is employed to characterize the effects of doping on the crystallinity in the ion-exchange doped PBTTT films with the three different counter anions. The calculated λ_x for TFO⁻, TFSI⁻, and TFMS⁻ are 0.83, 0.89, and 1.21 Å.

Figure 2a shows a representative GIWAXS image for a doped PBTTT film with TFSI⁻ as the counterion and the full set of GIWAXS data as a function of counterion size and conductivity are displayed in Figure S6 (Supporting Information). For all three counterions four orders of (h00) diffraction peaks are observed along q_z providing evidence that the PBTTT films retain a high level of crystallinity to the highest doping level. The lamellar spacing for neat PBTTT is calculated to be 20.8 Å, consistent with past reports for PBTTT-C14.^[21c] The (h00) diffraction peaks for the doped PBTTT films with maximum conductivities move to shorter scattering vectors by 0.05, 0.12, and 0.12 Å⁻¹ for TFO⁻ (Figure 6b), TFSI⁻ (Figure S6e, Supporting

a Ion exchange doping process



Materials

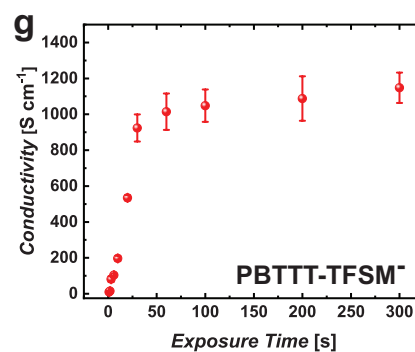
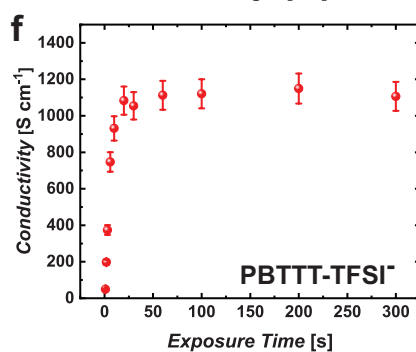
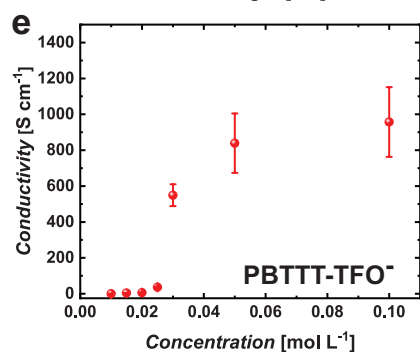
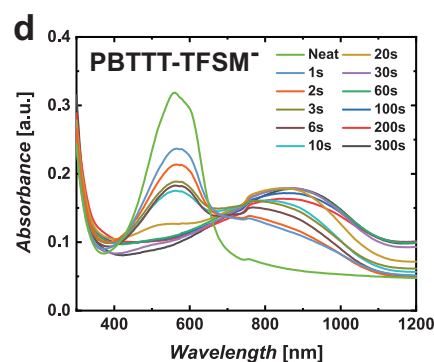
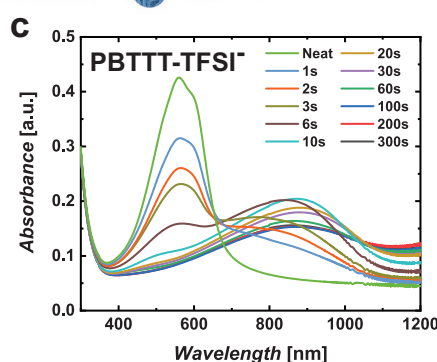
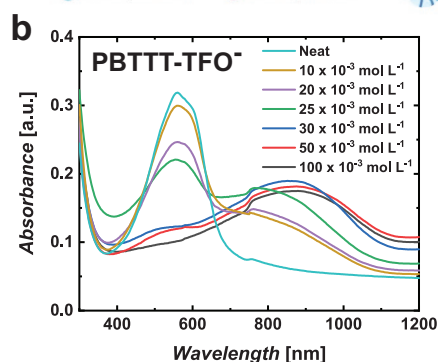
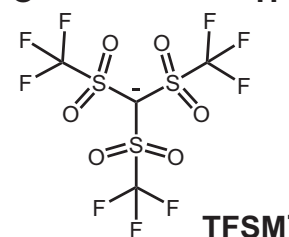
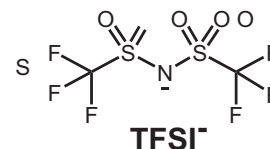
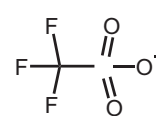
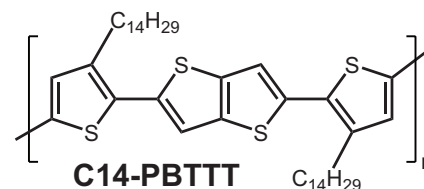


Figure 1. Characterization of ion exchange doped PBTTT. a) A schematic diagram of the ion exchange doping mechanism and of the materials used. b–d) UV–vis absorption spectra and e–g) the corresponding thin film conductivities for PBTTT-TFO⁻, PBTTT-TFSI⁻, and PBTTT-TFSM⁻, respectively, at different doping levels. To obtain different doping levels, exposure time to the dopant solution is varied for PBTTT-TFSI⁻ and PBTTT-TFSM⁻, while the concentration of dopant solution is varied for PBTTT-TFO⁻, to keep the doping conditions consistent with that for the preparation of multifunctional device samples. For PBTTT-TFSI⁻ and PBTTT-TFSM⁻, the doping solutions consisting of ion liquid/FeCl₃ were prepared at 100/1 × 10⁻³ mol L⁻¹ concentrations in acetonitrile; and for PBTTT-TFO⁻, the exposure time was fixed at 60 s. All optical and electrical characterization for each sample was collected on a single van der Pauw (vdP) chip (see the Supporting Information Section 1 for the device configuration) to keep the accuracy and consistency of experiments. *For the sake of brevity, the names of material systems do not include the oxidizing agent.

Information) and TFSM⁻ (Figure S6c, Supporting Information), corresponding to the expected expansion of the lamellar spacing $d_{(100)}$ of 22.8, 26.0, and 26.0 Å (top panel of Figure 2c), which is needed to accommodate the dopants in the side chain

regions of the lamellar structure. The observed equivalent expansion for PBTTT-TFSI⁻ and PBTTT-TFSM⁻ probably indicates a slightly lower doping level of PBTTT-TFSM⁻ than PBTTT-TFSI⁻ obtained under the same condition, due to

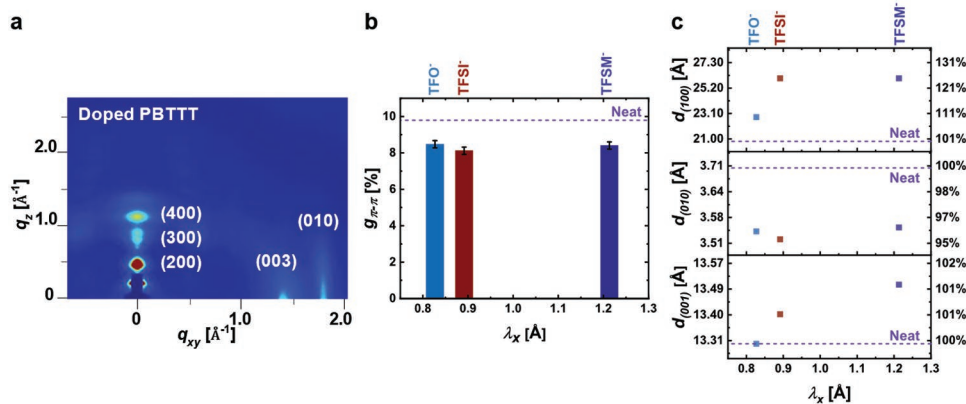


Figure 2. Grazing incidence wide-angle X-ray scattering (GIWAXS) results for PBTTT-TFO⁻, PBTTT-TFSI⁻, and PBTTT-TFSM⁻ doped to maximum conductivity. a) A representative 2D GIWAXS image for ion exchange doped PBTTT (Doping condition: 100×10^{-3} m BMP-TFSI/ 1×10^{-3} m FeCl₃, 60 s exposure time). b) Plot of π -stacking paracrystallinity $g_{\pi-\pi}$ versus ion size as defined by the smallest principal moment of the ionic gyration tensor λ_x . c) Plot of stacking distances $d_{(100)}$, $d_{(010)}$, and $d_{(001)}$ along the lamellar stacking, π - π stacking and backbone direction, respectively, versus λ_x . All the films were prepared under the same condition optimized to obtain the maximum VdP conductivity for each counterion: 100×10^{-3} mol L⁻¹ BMP-OTF/ 1×10^{-3} mol L⁻¹ FeCl₃, 60s exposure time for PBTTT-TFO⁻, 100×10^{-3} mol L⁻¹ BMP-TFSI/ 1×10^{-3} mol L⁻¹ FeCl₃, 300s exposure time for PBTTT-TFSI⁻ and 100×10^{-3} mol L⁻¹ DMPI-TFSM/ 1×10^{-3} mol L⁻¹ FeCl₃, 300s exposure time for PBTTT-TFSM⁻.

the lower ion-exchange efficiency for TFSM⁻ than TFSI⁻ in PBTTT.^[14b] Similarly, the lattice spacing $d_{(010)}$ along π - π stacking direction also shows an apparent decrease after doping by 0.16, 0.18, and 0.15 Å and for TFO⁻, TFSI⁻, and TFSM⁻ (middle panel of Figure 2c) reflecting an increased planarization of the backbone upon doping. This leads to better wavefunction overlap and interchain charge transfer.^[21c] By contrast, no significant change in the backbone repeat stacking distance is observed upon incorporating the counterions in all three cases (bottom panel of Figure 2c), which is similar to the sequentially doped PBTTT by F4-TCNQ.^[23a] Consistent with previous results the GIWAXS results indicate that the counterions mainly inhabit the alkyl side-chain zones without significantly disturbing the backbone packing.

The lattice paracrystallinity, which describes the cumulative structural disorder in an imperfect crystal, can also be extracted from the GIWAXS data. The paracrystallinity parameter g is the standard deviation in lattice spacing normalized by the average lattice spacing. In conducting polymers, paracrystallinity in the π -stacks largely affects the width of the density of states (DOS) tail and thereby is one of the key structural factors that affect the in-plane charge transport in FETs.^[31b,32] The π -stacking paracrystallinity $g_{\pi-\pi}$ for PBTTT-TFO⁻, PBTTT-TFSI⁻, and PBTTT-TFSM⁻ with the optimal conductivities is shown in Figure 2b. For all three doped systems, $g_{\pi-\pi}$ reduces by around 14–17% from a value of $9.8 \pm 0.2\%$ in the undoped state. This reduction is slightly more pronounced for PBTTT-TFSI⁻. The reduction in $g_{\pi-\pi}$ in PBTTT after doping suggests that all three ions studied here are incorporated into the polymer microstructure in an ordered manner, enabling polaron delocalization to enhance backbone planarity as previously observed in sequential molecular doping.^[23a,33]

In our previous work on PBTTT-TFSI⁻^[14a] we undertook a careful characterization by GIWAXS of the evolution of the polymer microstructure as a function of doping level/doping time. This showed that the conductivity only exceeds around 100 S cm^{-1} once the lamellar stacking distance $d_{(100)}$ expands significantly; at lower conductivities only a minor

expansion is observed. These findings are consistent with the GIWAXS characterization done here (Figure S6, Supporting Information). This suggests that at conductivity levels below $\approx 100 \text{ S cm}^{-1}$ doping mainly involves the amorphous regions of the film, while at higher conductivities also the crystalline domains become doped. This characteristic heterogeneity in the dopant distribution for conductivities $< 100 \text{ S cm}^{-1}$ is an important aspect that will need to be considered for the interpretation of the thermoelectric transport data discussed below.

2.3. S- σ Relationship and PF

To evaluate the thermoelectric performance in the three doped systems, the Seebeck coefficient was measured for different doping levels with conductivity ranging from 10^1 to 10^3 S cm^{-1} , and the corresponding room temperature power factor at each doping level was calculated accordingly. The S - σ -PF plot for PBTTT-TFO⁻, PBTTT-TFSI⁻, and PBTTT-TFSM⁻ are shown in Figure 3a and the maximum PF (PF_{max}) for each system is displayed in Figure 3b. We analyze the S - σ relationship with the Kang–Snyder model, which expresses the transport function as a power law (Equation (5.1) in the Supporting Information Section 5) with three key transport parameters: the exponent s , a transport parameter that may be used to classify the “type” of charge transport, the transport edge E_b , below which the carriers do not contribute to the conduction, and the transport coefficient σ_{E_0} , which is interpreted as a weighted mobility factor determining the conductivity and is believed to closely relate to the intrinsic carrier mobility of the system.^[11] A basic summary of Snyder’s model is given in the Supporting Information Section 5.

In general, we have not been able to fit the data well across the full conductivity range with a single set of parameters, s , E_b , σ_{E_0} . The data can be fitted well to $s = 3$ up to conductivities around 200 – 300 S cm^{-1} , but then follow an $s = 1$ model at higher conductivity values for all the three investigated

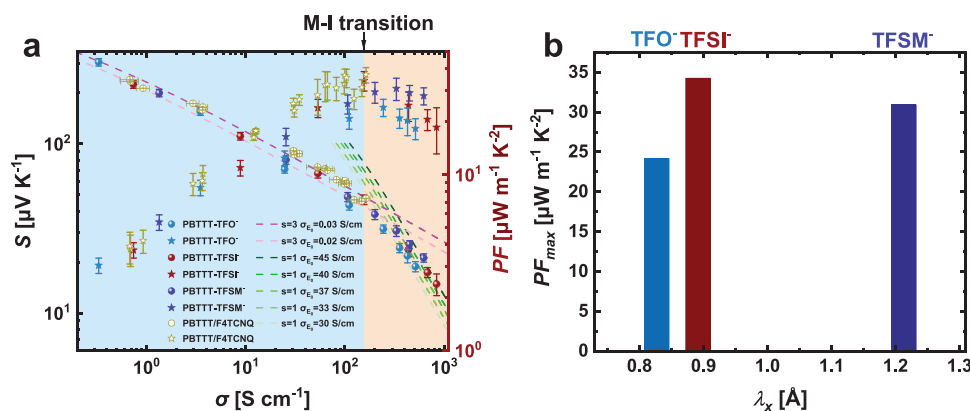


Figure 3. Thermoelectric properties of PBTTT-TFO⁻, PBTTT-TFSI⁻, and PBTTT-TFSM⁻ at 300 K. The conductivity (σ) dependence of the Seebeck coefficient (S) and power factor (PF) for PBTTT-TFO⁻, PBTTT-TFSI⁻, and PBTTT-TFSM⁻ are shown in (a). The S - σ - PF data reported in the literature^[20a] for PBTTT doped by a molecular dopant F4-TCNQ via a solution sequential doping process are also plotted in (a) for comparison. The scattered points are the measured data with the spheres and the stars representing S and PF , respectively, and the fitting results are displayed as dashed lines. The PF_{\max} at RT for PBTTT-TFO⁻, PBTTT-TFSI⁻, and PBTTT-TFSM⁻ are shown in (b).

systems (Figure 3a). Such a consistent transition of S - σ curvature indicates a change of charge transport mechanism from a non-/semimetallic to a fully metallic regime and an insulator-to-metal transition, which is discussed in more detail in Section 2.4 below based on the temperature dependence of σ and S . The PF_{\max} for PBTTT-TFO⁻, PBTTT-TFSI⁻, and PBTTT-TFSM⁻ appears around the insulator-to-metal transition as shown in Figure 3a, which is consistent with previous studies reporting the strong correlation between the insulator-to-metal transition and optimal thermoelectric performance in polymer systems that can approach the degenerate regime via doping.^[13,15] The PF_{\max} for PBTTT-TFSI⁻ is $34.2 \pm 4.3 \mu\text{W m}^{-1} \text{K}^{-2}$, which is slightly higher than the values for PBTTT-TFSM⁻ ($30.9 \pm 4.5 \mu\text{W m}^{-1} \text{K}^{-2}$) and PBTTT-TFO⁻ ($24.2 \pm 2.7 \mu\text{W m}^{-1} \text{K}^{-2}$), respectively (see Figure 3b).

All the data fit well to $s = 3$ with σ_{E_0} between 0.02 to 0.03 S cm^{-1} before the transition occurs (see Figure 3a), and, interestingly, this set of fitting parameters is also close to those for nonion exchange doped PBTTT films prepared by molecular doping with F4-TCNQ that reach conductivities up to 200 S cm^{-1} as reported by Kang et al.^[20a] (see the data marked golden yellow). Accordingly, the PF at low conductivities also shows a nearly identical power law dependence of σ for all the three systems. Such universality of the S - σ - PF relationship observed probably indicates that the transport in PBTTT-TFSI⁻, PBTTT-TFSM⁻, PBTTT-TFO⁻ as well as solid-state diffusion doped PBTTT/F4-TCNQ is very similar at low conductivities, which is also reflected in the consistency of the thermal activation energy E_A for the electrical conductivity at room temperature (σ_{RT}) (Figure 5a) the (morphology-related) transport barrier $W\gamma$ generated from the analysis by the Kang-Snyder model (Figure 5b). Those universal charge and thermoelectric transport phenomena in ion exchange doped PBTTT will be discussed further in Section 2.5.

By contrast, the three doped systems show different features in the S - σ relationship when the doping level and the conductivity keep increasing beyond the insulator-to-metal transition, where the transport parameter s decreases from 3 to 1. As shown in Figure 3a, the transport coefficient/weighted mobility σ_{E_0}

for the data fitting with $s = 1$ model moves from 45 to 30 S cm^{-1} with decreasing the counterion size. Consistent with this, PBTTT-TFSM⁻ exhibits the weakest PF drop-off in the high σ region, while the PF for PBTTT-TFO⁻ drops the fastest. It is possible that this relatively weak counterion size dependence of the S - σ - PF relationship for the heavily doped PBTTT could presumably arise from the microstructural difference created by different counterions. Our previous work^[14b] has pointed out that the paracrystallinity $g_{\pi-\pi}$ plays a dominant role in controlling the charge transport properties at high doping levels as the counterion induced Coulomb landscape smooths out with adequate ions accommodated in the side chain region. Apart from the subtle differences in paracrystallinity (Figure 2b) we also detected slight differences in the intensity distribution of the (h00) peaks, indicating differences in microstructural packing, in PBTTT-TFO⁻ compared with the other polymers (Figure 2a; and Figure S6, Supporting Information). Such subtle microstructural differences could well explain the differences in the transport behavior in this regime.^[14b]

As observed in our previous work,^[14a] the peak in PF corresponds to the conductivity where counterions start to be incorporated into crystalline domains of the polymer, which occurs at conductivities around 100 S cm^{-1} . The incorporation of counterions into the crystallites that sets in around this conductivity level likely allows for delocalized metallic states within crystalline domains, whereas at lower conductivity polarons are likely confined primarily to more disordered regions in grain boundaries. A smaller ion like TFO⁻ should begin intercalating into the crystallites at lower doping levels, as evident from the higher exchange efficiency for TFO⁻.^[14a] This could potentially push the metal-insulator (M-I) transition (an electronic phase transition from a metallic to an insulating state) to a point earlier in the S - σ curve as observed here, leading to a lower PF . A more detailed future study will be required to clarify this. However, despite these relatively subtle differences between the three ions the data in Figure 3 suggest that across the entire range of conductivities investigated here the thermoelectric properties are broadly independent of ion size.

2.4. Temperature Dependence of S and σ in Ion Exchange Doped C14-PBTTT

To further investigate the transport physics, we also measured the conductivities and Seebeck coefficients on the same samples as a function of temperature. As shown in Figure 4a–f, the temperature dependence of σ becomes weaker when increasing doping level for all three systems. At the highest doping levels, approaching 1000 S cm⁻¹, the conductivity is only weakly temperature dependent. For instance, PBTTT-TFSI⁻ sample B maintains a conductivity up to 682 S cm⁻¹ at 5 K, which is ≈60% of the conductivity at room temperature (RT) (Figure 4e). To better understand the charge transport mechanism in these systems, we performed a Zabrudskii analysis (see the Supporting Information Section 6 for more information) to the temperature dependence of conductivity. In the Zabrudskii analysis, the reduced activation energy

$W = \text{dln}\sigma/\text{dln}T$ is plotted against temperature on a log–log scale. A positive slope in a plot of $\log W(T)$ versus $\log T$ at low T usually indicates the emergence of a metallic state; while insulating, hopping behavior manifests itself as a negative slope in a plot of $\log W(T)$ versus $\log T$ at low T .^[34] The intermediate regime in which the reduced activation energy is temperature independent is often referred to as the critical regime. In general, the temperature dependence of conductivity for all the three systems evolves from hopping-like (reduced activation energy decreasing with increasing temperature) to near-metallic (reduced activation energy near temperature independent or even increasing with increasing temperature) as the doping level increases. Such a trend is evidenced by the slope of the Zabrudskii plot at low temperature changing from negative to positive (PBTTT-TFSI⁻, Figure 4b) or almost constant (PBTTT-TFSM⁻ and PBTTT-TFO⁻, Figure 4a,c) as the samples become more conductive.

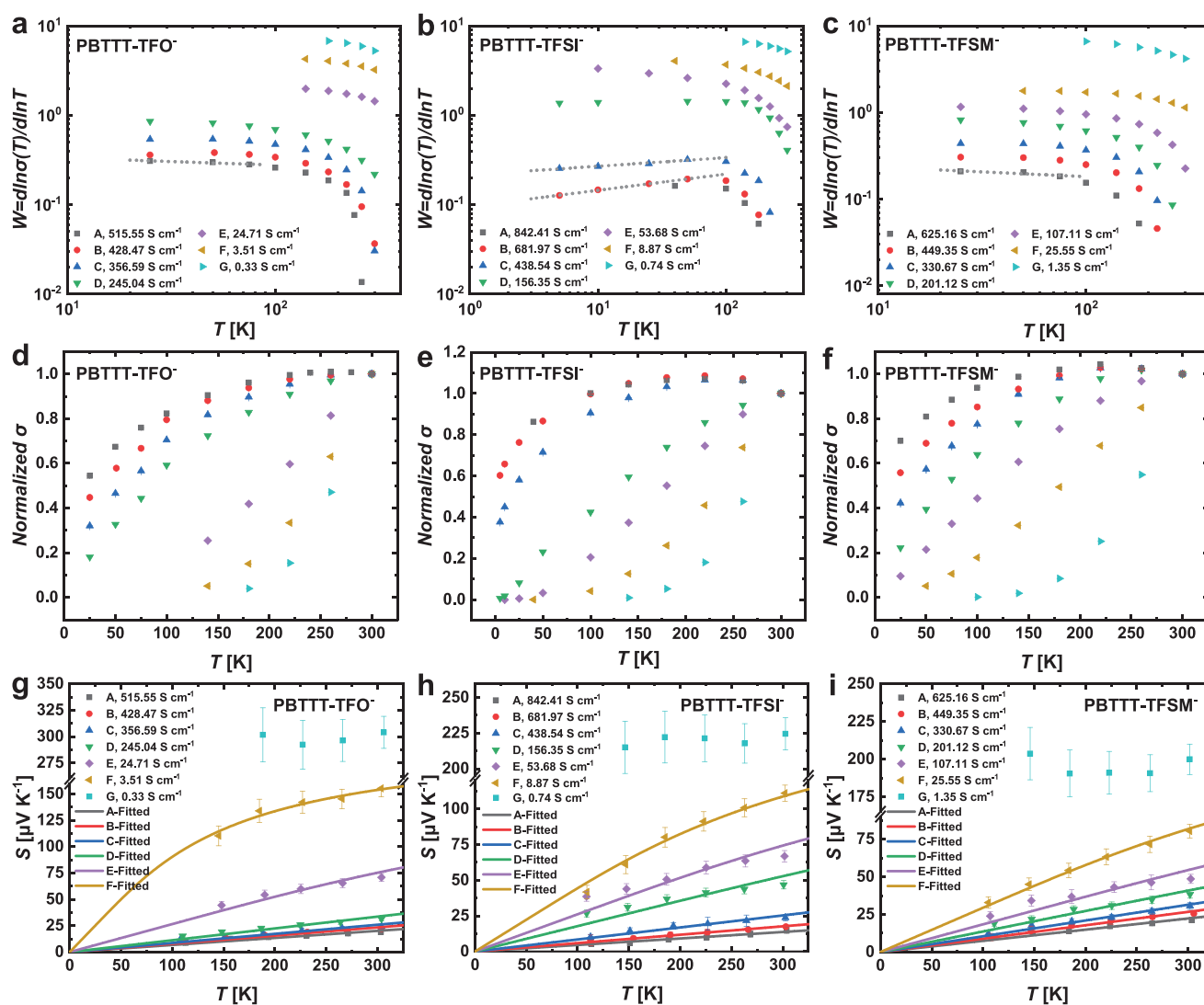


Figure 4. Temperature dependence of conductivity (σ) and Seebeck coefficient (S) in PBTTT-TFO⁻, PBTTT-TFSI⁻ and PBTT-TFSM⁻ at different doping levels. The Zabrudskii analysis plot for the $\sigma(T)$ results for PBTTT-TFO⁻, PBTTT-TFSI⁻, and PBTT-TFSM⁻ are shown in (a), (b), and (c), respectively. The $\sigma(T)$ results for PBTTT-TFO⁻, PBTTT-TFSI⁻, and PBTTT-TFSM⁻ are shown in (d), (e), and (f), respectively. The $S(T)$ results and the fitted data for PBTTT-TFO⁻, PBTTT-TFSI⁻, and PBTT-TFSM⁻ are shown in (g), (h), and (i), respectively.

Such an evolution in the temperature dependence of conductivity as a function of the doping level supports the argument that there is a transition between transport regimes at certain intermediate conductivity, as deduced from the analysis of the S - σ relationship in Section 2.3. The positive slopes of the Zabrudskii plot only appear in the PBTTT-TFSI⁻ samples with the conductivity above the transition point to the $s = 1$ regime (around 100 S cm⁻¹). This indicates that the PBTTT-TFSI⁻ system (Figure 4b) can approach the metallic side of the metal-insulator transition, while the highly doped PBTTT-TFSM⁻ and PBTTT-TFO⁻ samples just reach the critical regime (Figure 4a,c). We conclude that PBTTT-TFSI⁻ exhibits the most metallic transport among the three investigated systems, which is consistent with the lowest paracrystallinity for PBTTT-TFSI⁻ extracted from the GIWAXS characterization (Figure 2b). This observation is also consistent with the evolution of polaron delocalization that will be discussed below based on infrared spectroscopy.

The temperature dependence of Seebeck coefficients (shown in Figure 4g,h,i) further confirms the universal evolution of charge transport from hopping to metallic regime as the doping level increases. The Seebeck coefficients are nearly temperature independent for the samples with a conductivity around 1 S cm⁻¹, which can be explained by the Efros-Shklovskii VRH (ES-VRH) model for doped polymers.^[35] For the samples with higher conductivities, the Seebeck coefficients show either $T^{1/2}$ or linear T dependence.

For a deeper understanding of $S(T)$, we fitted those data with a model proposed by Akrap et al.^[36] that considers a simple free-electron metal with a parabolic density of states and an energy dependent scattering time (Equation (71) in the Supporting Information Section 7). The model reproduces the linear temperature dependence of the Seebeck coefficient that is expected from the Mott formula in a regime at high doping levels when the reduced Fermi energy $\eta_F = E_F/k_B T \gg 1$. At lower doping levels, the Fermi energy becomes comparable to the thermal energy and this leads to a nonlinear temperature dependence observed in Figure 4g,h,i. From the fits we can estimate values of the Fermi energy for the different samples (Figure S8, Supporting Information). This analysis shows that for a given conductivity value the samples with different ions exhibit very similar values of Fermi energy, i.e., their carrier concentrations are likely to be very similar, in particular in the intermediate conductivity regime around 100 S cm⁻¹. The least conductive samples (see the blue dots in Figure 4d,e,f) cannot be fitted with the model, in this regime a different framework for polaron hopping transport^[22,35b] needs to be applied, but this is not further considered here.

2.5. Ion Size Dependence of Thermoelectric Transport in Intermediate Conductivity Regime

The S - σ - PF relationship discussed in Section 2.3 and the temperature dependence of S and σ addressed in Section 2.4 have together provided solid evidence that the three investigated ion exchange doped PBTTT share very similar charge and thermoelectric properties despite the varying counterion sizes across the full range of conductivities/doping levels investigated here.

This is consistent with recent works by Thomas et al.^[25] and Jacobs et al.,^[14b] who observed negligible ion-size effects on conductivity at high doping levels ($>10^{20}$ cm⁻³). However, at low doping levels ($<10^{18}$ - 10^{19} cm⁻³), we still expect strong ionic trapping, as described by Arkhipov et al.,^[24a] to prevail, leading to a strongly increasing conductivity and power factor with increasing ionic size. The transition between these two regimes is unclear, however the observation of ion-size independent behavior down to conductivity <1 S cm⁻¹ suggests that this transition point must happen at a much lower conductivity than we might intuitively expect.

To further explore this universal behavior, we now focus in more detail on the intermediate conductivity samples with room temperature conductivities between 10^{-1} and 10^2 S cm⁻¹. In this regime, the conductivity can be described by an Arrhenius-type dependence near room temperature with $\sigma(T) \propto \exp(-E_A/K_B T)$, where E_A is the thermal activation energy and K_B is the Boltzmann's constant.^[37] We obtain the E_A near room temperature for different room temperature conductivities σ_{RT} (see Figure S9 for the examples of E_A extraction, Supporting Information).

Figure 5a shows that σ_{RT} of all the three systems is strongly correlated with E_A in a broad range of conductivities ranging from 10^{-1} to 10^2 S cm⁻¹, which is a commonly observed transport phenomenon for doped organic semiconductors.^[38] However, our results in Figure 5a suggest that the correlation between σ_{RT} and E_A has a negligible dependence on the counterion size in this regime. This is further evidence for an absence of counterion size dependence of charge transport, not just at high conductivity (≈ 1000 S cm⁻¹), but also at lower conductivities (down to <1 S cm⁻¹), and is fully consistent with the S - σ dependence discussed in Figure 3.

A similar conclusion is reached when analyzing the activation energy W_γ in the Kang-Snyder model, which describes the energy barrier for the percolation for transport between the ordered regions and is defined by the equation $\sigma_{E_0} \propto \exp\left[-\left(\frac{W_\gamma}{K_B T}\right)^\gamma\right]$ ^[11] (see the Supporting Information Section 5 for more details). We obtain W_γ for each system in the intermediate conductivity regime, where the S - σ relationship can be described by the $s = 3$ model, from the linear fitting of $\ln \sigma_{E_0}$ versus $T^{-1/2}$, as displayed in Figure 5b). PBTTT-TFO⁻, PBTTT-TFSI⁻, and PBTTT-TFSM⁻ exhibit W_γ values of 504 ± 130 , 484 ± 65 , and 470 ± 64 meV, respectively. These values are identical to within the measurement error; therefore, it is reasonable to conclude that the transport barrier W_γ also has negligible dependence on the counterion size even at below a conductivity of 1 S cm⁻¹. Since W_γ is sensitive to the structural disorder, we would expect a similar degree of structural disorder to determine the transport in each system at these low conductivities.

These observations are unexpected from the classic transport theory for lightly doped OSCs, which highlights that at low doping concentrations ($<10^{18}$ - 10^{19} cm⁻³), the Coulomb traps introduced by dopant ions play a leading role in determining the charge transport and smaller counterions tend to have larger E_A as stronger interaction between the OSC and counterions has to be overcome to generate a free charge from the ion pair.^[8b,38,39]

However, we can rationalize these results consistently by examining the carrier density at relatively low conductivity.

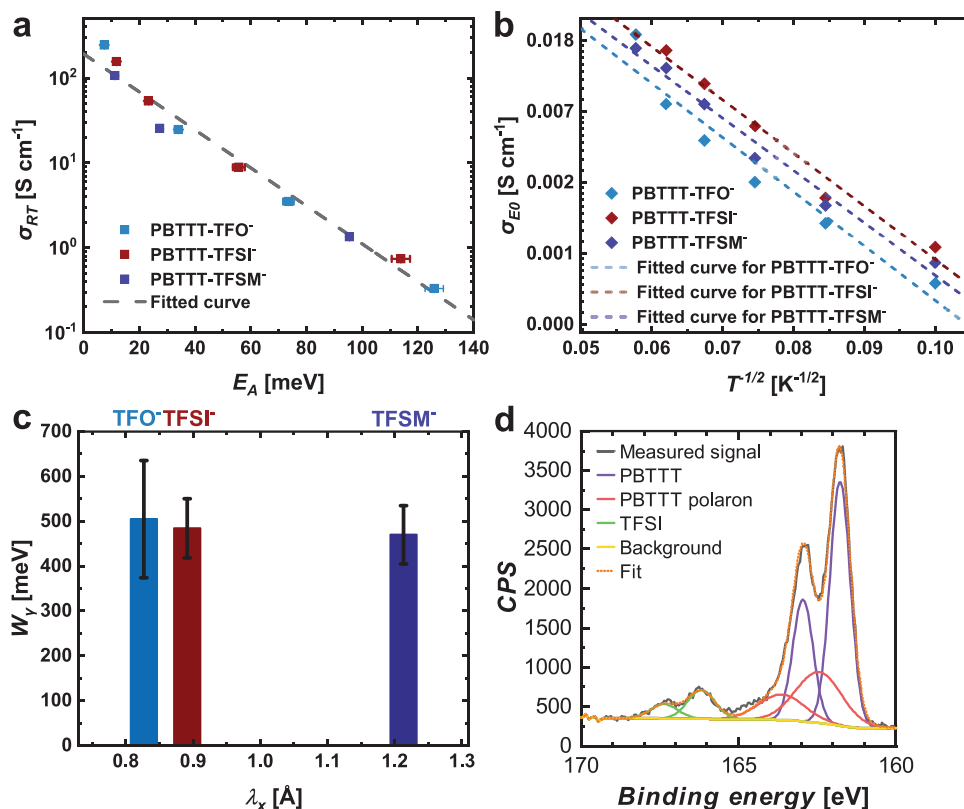


Figure 5. Universal Charge and thermoelectric transport properties in ion exchange doped PBTTT at conductivity $<100 \text{ S cm}^{-1}$. a) Plot of conduction activation energy versus electrical conductivity, showing a consistent exponential relationship between the room-temperature conductivity σ_{RT} thermal activation energy E_A for PBTTT-TFSI $^-$, PBTTT-TFSM $^-$, and PBTTT-TFO $^-$. The black dashed line is generated by a linear fitting of the displayed data. b) Arrhenius plot of $\ln\sigma_{E0}$ versus $T^{-1/2}$ to extract the transport barrier W_γ with the W_γ values for each system shown in (c). γ is taken as 1/2 as widely chosen for polymers. The R-square values for the linear fitting of $\ln\sigma_{E0}$ versus $T^{-1/2}$ are 0.98, 0.98, and 0.94, respectively. The dashed lines are generated by a linear fitting of the displayed data. d) X-ray photoemission spectroscopy (XPS) spectra of a PBTTT-TFSI $^-$ film doped to a conductivity of 1.9 S cm^{-1} , showing the S 2p edges.

Figure 5d shows a S 2p XPS spectrum of a PBTTT film doped to a conductivity of 1.9 S cm^{-1} . The carrier density in this film, determined from the concentration of TFSI ions, is $1.9 \times 10^{20} \text{ cm}^{-3}$, equivalent to a concentration of about 1 dopant per 5 PBTTT repeat units (details on the XPS measurements can be found in the Supporting Information Section S10). This is a surprisingly high carrier density—at maximum doping level (≈ 1 ion per monomer)^[14b] PBTTT-TFSI $^-$ achieves a conductivity over 500 times higher, however the carrier density of these highly conducting samples is less than 5 times higher. We have argued above based on structural characterization that up to conductivities of $\approx 100 \text{ S cm}^{-1}$ the doping is heterogeneous and occurs preferentially in the amorphous domains of the polymer film. This means that in the amorphous domains the local carrier concentration is even larger than $1.9 \times 10^{20} \text{ cm}^{-3}$. At such high doping levels it is not surprising that we do not observe a marked ionic size dependence, as the argument we proposed previously—that polaron delocalization is significantly greater than the distance between ions—should still hold.

For completeness we also performed Hall measurements at different doping levels, but as discussed in the Supporting Information Section S9 the interpretation of these measurements is not straightforward and they are therefore not taken into further consideration here.

2.6. Infrared Absorption Spectra of Polarons as a Function of Ion Size

The observation that at relatively low conductivity doping is heterogeneous while the average carrier density is already high requires explanation. Recent theoretical work by Qarai et al.^[29] has suggested that in bipolaron states consisting of two polarons and two ions, the total energy of these bipolaron states is lower than two spatially separated polaron-ion pairs—that is, that dopant clustering should be energetically favorable. This prediction is consistent with previous studies in similar systems, such as PB2T-TEG, where a doping-induced phase transition was observed via a sharp boundary between doped and undoped phases in scanning probe microscopy.^[40] As discussed above in our previous work in PBTTT-TFSI $^-$ we observed similar behavior: at conductivity below $\approx 100 \text{ S cm}^{-1}$, we observed only a slight expansion of the PBTTT lamella, which we interpreted as preferential doping of disordered regions, while at higher conductivity, we observed a large increase in the lamellar stacking distance, indicative of ion insertion into the lamellar region in the crystalline domains. The same trend is observed in our GIWAXS data here (Figure 2; and Figure S6, Supporting Information). Our interpretation is that we initially dope grain boundaries or other disordered polymer regions, and that

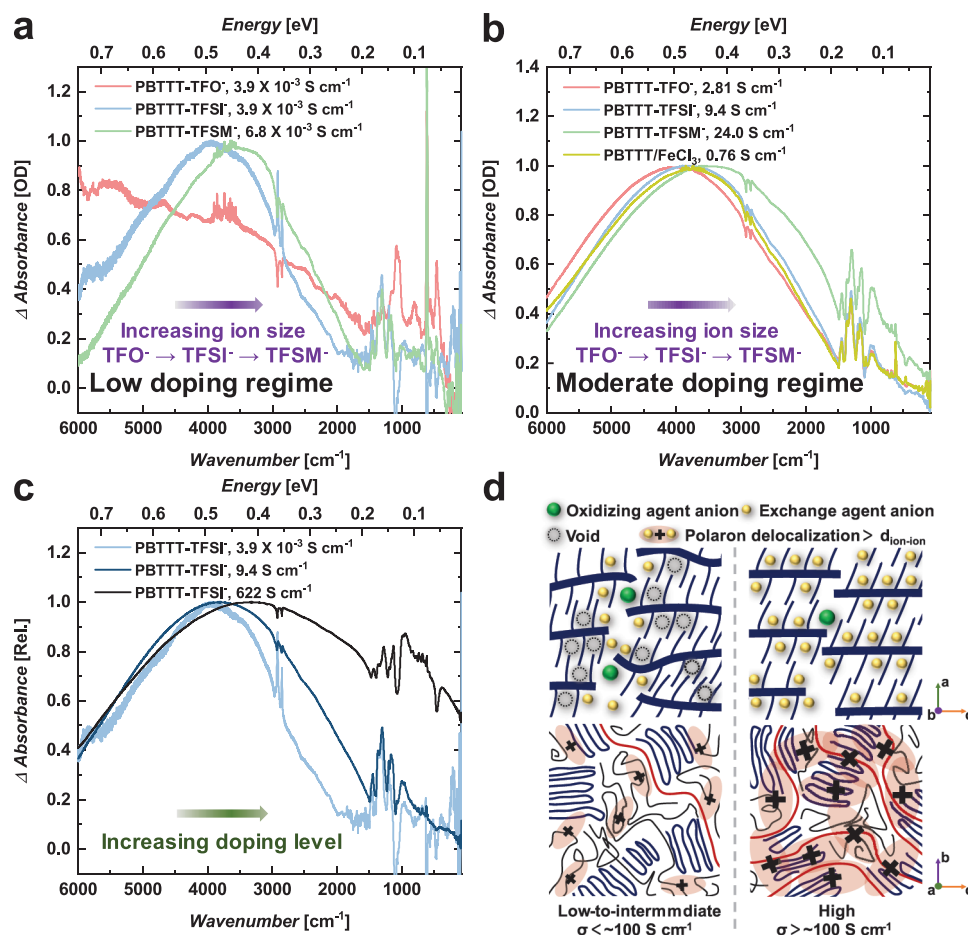


Figure 6. Infrared spectroscopy of polarons at different conductivities. The normalized mid-IR spectra for ion exchange doped PBT TT with different ions with conductivity on the order 10^{-3} S cm^{-1} a) and conductivity on the order 1–10 S cm^{-1} b). c) The doping level dependence of mid-IR differential (doped minus undoped) spectra for PBT TT-TFSI $^{-}$. All the samples were doped with 100 mM electrolyte with variable phosphomolybdic acid (PMA) concentrations with a fixed exposure time of 60 s to ensure a high exchange efficiency at doping levels below the range where ion intercalation into crystallites occurs. Further details of doping conditions are given in the methods. Note that due to experimental limitations it is not possible to exactly match doping levels between samples within each regime. d) Illustration of film microstructure, dopant habitat, polaron delocalization and transport pathways in ion exchange doped PBT TT at low-to-intermediate conductivity (<100 S cm^{-1} , left panel) and high conductivity (>100 S cm^{-1} , right panel) regimes. In both displayed doping regimes, the doping level is high enough that the polarons are delocalized over a distance greater than the distance between the ions.

transport through these doped, disordered regions limits the electrical conduction until the electrical conductivity reaches values around 100 S cm^{-1} when the crystalline domains become doped as well and the doping becomes more homogeneous.

To better understand the degree of polaron delocalization as a function of doping level, we turn to IR spectroscopy. Doping-induced polarons display strong mid-IR absorbances that shift depending on delocalization. Therefore, shifts in the peak positions of the polaron band can provide evidence for the degree of localization, for instance by ionic trapping or disorder. In our previous study, we saw evidence for reduced ion exchange efficiency in the early stages of doping before crystalline domains become doped.^[14a] To ensure our IR spectra accurately reflect the polaron localization in the presence of the exchanged anion rather than FeCl_4^{-} , we instead used phosphomolybdic acid (PMA) as the dopant in these samples. PMA is an extremely large and is unable to diffuse into the bulk of PBT TT on typical

doping timescales (1 min).^[41] The addition of an electrolyte to these doping solutions leads to rapid doping, indicating that in this system electrolyte anions are strongly kinetically favored, resulting in high exchange efficiency even at very low doping levels.

As shown in **Figure 6a,b**, the spectra of PBT TT ion-exchange doped with PMA and each electrolyte exhibit two peaks, the so-called “B” or P1 peak, as referred to in ref.,^[29] around 0.4–0.7 eV, and the “A” peak around 0.1 eV. The latter is superimposed with sharp vibrational transitions due to charge-induced infrared-active vibrations which are not discussed here further. The “B” peak shows a strong counterion size dependence at low doping levels ($\sigma \approx 5 \times 10^{-3}$ S cm^{-1} , n (charge concentration) $\approx 10^{17}$ to 10^{19} cm^{-3}), while its variation between ions becomes smaller at the low end of the conductivity range in our transport measurements ($\sigma \approx 2\text{--}25$ S cm^{-1} , $n \approx 2\text{--}3 \times 10^{20}$ cm^{-3}). The redshifted polaron band with increasing doping density is

indicative of increased polaron delocalization. This convergence in polaron spectra in the low conductivity regime (on the order of 1–10 S cm⁻¹) is consistent with the absence of ion-size effects in the transport data reported above, as it indicates a similar level of polaron delocalization across all three ions.

Notably, these spectra are still much more localized than we observe at high conductivity (Figure 6c; and Figure S11, Supporting Information). This localization effect is entirely consistent with uniformly higher disorder in doped domains. We see further evidence for this picture of preferential doping of disordered regions in the doping level dependent spectra of PBTTF-TFSI⁻ in Figure 6c. From the lowest conductivity (0.005 S cm⁻¹) to moderate conductivity (9.4 S cm⁻¹), we observe a slight broadening and red shift, however the spectra remain fairly similar. However, at higher conductivity (622 S cm⁻¹), where the carrier density cannot be more than a factor of 4–5 times higher, we observe a strong red shift and the growth of a large low-energy shoulder peak. According to the Holstein-based model developed by Spano^[29,42] the observed doping level-dependent redshift of the mid-IR peak P1 with a concomitant increase in the intensity of the lower-energy “A” peak between 300 and 1500 cm⁻¹ is indicative of charge delocalization and therefore must derive from carriers within ordered crystalline domains. These observations are fully consistent with the significant reduction in pi–pi stacking distance and expansion of the lamella, which coincided with a simultaneous redshift and increase in the A peak in FTIR spectra, observed by GIWAXS in our previous work on PBTTF-TFSI⁻^[14a] and here (Figure S6, Supporting Information). These spectra therefore clearly suggest that in the low-intermediate conductivity regime <100 S cm⁻¹, we preferentially dope disordered regions of the film (e.g., grain boundaries or other disordered sites within crystallites, Figure 6d left panel). This is fully consistent with literature results on ionic liquid gated P3HT films.^[43] However, our spectroscopic results also provide direct evidence that in this regime the majority of polarons remain localized in these disordered regions, not within crystallites. In the literature, it has been suggested that at interfaces between semicrystalline polymer films and polymeric ionic liquids with tethered ionic units the resulting polarons may be able to migrate preferentially into the crystalline domains with shallower highest energy occupied molecular orbital (HOMO) level.^[44] In our bulk doped PBTTF, the spectroscopic results allow us to exclude this possibility. If the carriers were already located in the crystalline domains at low-intermediate conductivities it would be difficult to explain the dramatic change in the IR spectrum when the crystalline domains become doped (Figure 6c). The negative dopant ions in the amorphous domains generate an average attractive potential with a depth on the order of $V = k/\epsilon r \approx 1$ eV, where $k = 14.4$ eV Å e⁻², $\epsilon \approx 3$ and $r = 5$ Å, a typical dopant-polaron distance. The resulting potential well between the doped amorphous regions and the undoped crystalline domains is expected to prevent the majority of polarons from migrating into the crystalline domains in this low-intermediate conductivity regime. Charge transport is therefore dominated by the microstructural disorder of these doped amorphous regions.

We stress that the absence of ion size effects and the confinement of carriers to disordered regions are not contradictory. Although carriers are confined to the amorphous domains, the

doping density within this region is already sufficiently high that the polaron wavefunctions start to overlap and multipolaron states are formed in these disordered regions of the polymer film. As argued,^[29] in such multipolaron states the wavefunctions tends to be more delocalized, allowing effective averaging over the electrostatic potential landscape created by the ions and as a result the transport becomes ion size independent already in this regime. Once these sites are filled, we begin to incorporate ions into the ordered crystalline regions (Figure 6d right panel), leading to a strong increase in conductivity and thermoelectric performance, evidence for delocalization in the IR spectrum of the polarons, and signatures of metallic states in the temperature dependent charge transport of these films. While we expect similar behavior in other polymer/dopant systems, we expect that the choice of which region dopes first will depend both on whether the doping process is kinetically or thermodynamically controlled, as well as on the crystallinity of the polymer and the size of the dopant ion. For instance, in a thermodynamically controlled doping process, there will be a competition between the energetic cost of inserting a dopant ion into a crystalline domain and the HOMO level difference of the amorphous and crystalline domains. Doping a weakly crystalline material with a very small ion therefore might lead to the opposite behavior, with preferential doping of crystalline domains.

To rationalize these trends seen in the experimental infrared spectra further we also calculated infrared absorption spectra of multipolaron states for a model polymer system. Realistic calculations of infrared spectra at high doping concentrations are very challenging as it is not sufficient to simulate isolated polarons localized around individual dopant anions, but instead multipolaron states stabilized by multiple counterions on the same segment of the polymer need to be considered. Our model for such multipolaron states, which extends our earlier work,^[29] is based on the simplified polymer-anion geometry, where anions are positioned on both sides of the polymer chain as illustrated in Figure 7a for a tetrapolaron complex. The model is based on a site Hamiltonian parametrized for P3HT, in which each unit in Figure 7a represents a thiophene ring, while the experimental spectra were obtained on the related polymer PBTTF. Details of the calculation can be found in the Experimental Section as well as in ref. [45]. The figure shows that the normalized absorption spectrum redshifts with the size of the multipolaron complex, i.e., as n increases from 1 to 4 in a n -polaron complex (Figure 7b). This is because the holes delocalize more efficiently – due to repulsion – in a tetrapolaron versus a polaron. This trend is an extension of our earlier work on polarons and bipolarons^[29] and is also consistent with the infrared measurements of Enengl et al. in electrochemically doped P3HT.^[46] The spectrum appears to converge by the tetrapolaron. Figure 7b,c compares a set of spectra for two different values of d_{an} – the distance between the anion and the chain. As d_{an} increases the spectrum dramatically redshifts for the polaron but hardly at all for the tri- and tetrapolaron. This ultimately derives from a flattening of the Coulomb well in going from polaron to tetrapolaron. The simulations demonstrate that the spectrum is expected to be almost independent of ion radius for high doping concentrations (where tetra and higher-polarons are dominant) but not for low doping concentrations

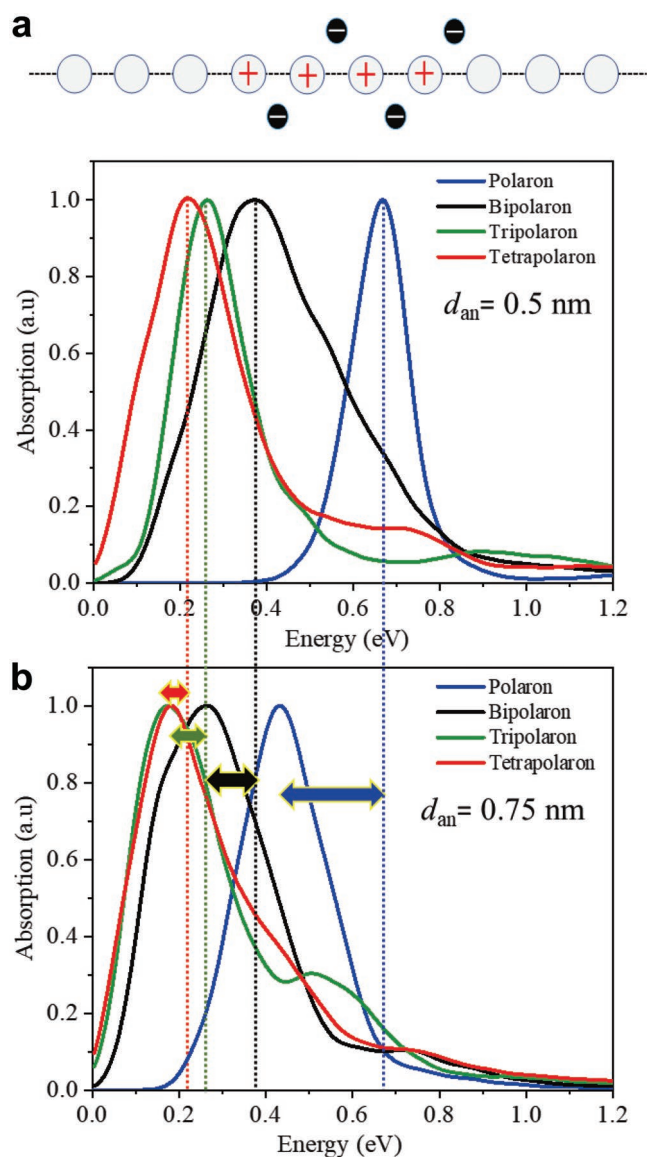


Figure 7. Simulation of the infrared absorption spectrum of polarons in a model polymer chain. a) Schematic diagram of a tetrapolaron complex consisting of four negatively charged counterions (and four mobile holes) along a segment of a model P3HT polymer chain, where each circular unit represents a thiophene ring with nearest-neighbor separation of 0.4 nm. The anions are located at a distance d_{an} from the polymer backbone in the lamellar region. Note: this model was parameterized for P3HT, however we expect qualitatively similar behavior in PBTTT. b,c) Calculated normalized absorption spectra of polaron, bipolaron, tripolaron, and tetrapolaron states on a polymer chain with 20 thiophene units for $d_{an} = 0.5$ nm b) and $d_{an} = 0.75$ nm c). The dashed lines indicate the positions of the absorption peaks in (b). The spectra redshift with increasing multipolaron complex size and with increasing d_{an} .

(dominated by single polarons). This is qualitatively consistent with our experimental observations in Figure 6. The simulated spectra in Figure 7b,c support our conclusion above, that already at moderate conductivities the regions of the film that contain these polarons are sufficiently highly doped that delocalized, ion-size independent multipolaron states are formed. We caution that a more quantitative comparison between the

experimental and simulated spectra is unfortunately not possible at present. This is because of a number of simplifications that had to be made in the model. In addition to being parameterized for P3HT (and not PBTTT), vibronic coupling could not be included since the basis set size became too large for tri- and tetrapolarons. As a result the spectra do not contain the low-energy, "A" peak,^[29] but only the "B" peak (P_1 peak), which is known to be relatively insensitive to vibrational coupling.

3. Conclusion

In this work, we have investigated the important question of Coulombic trapping in doped conjugated polymers by investigating the role of counterion size across a wide range of electrical conductivities using ion-exchange doped C14-PBTTT as a controlled model system. We observed universal charge and thermoelectric transport features with weak counterion size dependence. A transition from $s = 3$ to $s = 1$ in the S - σ plot at RT was observed for all ion sizes, accompanied by the emergence of PF_{max} . The temperature dependences of conductivity and Seebeck coefficient demonstrate a strong correlation between such a transition in the S - σ relationship and the metal-insulator transition, beyond which the metallic signatures, including a negative temperature coefficient of $\sigma(T)$ near room temperature and a linear dependence of $S(T)$ for the heavily doped samples. We find that Coulomb trapping between the charge carriers and their counterions plays a nearly negligible role, not just at the highest conductivities approaching 10^3 S cm^{-1} as observed previously, but, surprisingly, even at intermediate conductivities in the range between 10^{-1} and 10^2 S cm^{-1} . XPS measurements reveal a surprisingly high carrier density to be present already in this regime. Based on evidence from GIWAXS and IR spectroscopy, we conclude that the absence of ion-size effects in the thermoelectric transport properties in this intermediate conductivity regime derives from a high carrier density, that arises locally because the films are not uniformly doped, but the disordered regions and grain boundaries are doped preferentially. Our results suggest an effective strategy for enhancing thermoelectric performance of such semicrystalline conjugated polymers: If the dopant ions could be spread more uniformly throughout the polymer film, it should be possible to achieve a high conductivity at lower doping levels where S is higher and κ is lower, potentially improving thermoelectric power factors and performance significantly. Our findings provide important new insights into the structure–property relationship in ion-exchange doped conjugated polymers and stimulate rational doping rules to control the charge and thermoelectric transport in polymer systems for TE applications.

4. Experimental Section

Sample Preparation: C14-PBTTT was dissolved in 1,2-dichlorobenzene (DCB) with a concentration of 10 mg mL^{-1} and heated up to 120 °C until full dissolution was achieved. The hot solutions were then filtered by 0.45 μm PTFE filters with glass syringes and annealed at 120 °C for an hour before cooling down to 80 °C for the film coating. The polymer films were deposited via spin-coating on different substrates, including glass (devices for transport measurements & UV-vis spectroscopy)

and silicon (GIWAXS & FTIR). Those substrates were pre-cleaned by sonication in Decon 90 detergent, DI water, acetone, and isopropanol before oxygen plasma ashing for 10 min at 300 W before being transferred into a nitrogen glovebox for spin-coating. The substrates and glass pipettes were maintained at 90 °C to minimize the temperature difference. The PBTTT-C₁₄ films were spin-coated at 1500 rpm for 120 s to provide a thickness of around 40 nm and annealed at 180 °C for 20 min after which the samples were gradually cooled down to room temperature.

Doping was achieved by the ion exchange doping method (see Figure 1a for a conceptual illustration). The oxidizing agents FeCl₃ and PMA and ionic liquids, BMP-TFSI, DMPI-TFSM, and BMP-OTF, were all purchased from Sigma-Aldrich LLC. The fresh oxidizing agent solution and ionic liquid solution were both prepared in acetonitrile (ACN) separately before mixing them together. Each concentration is fixed according to the expected ratio of oxidizing agent and ionic liquid and the required amount of solution to dope the film. The oxidizing agent and ionic liquid are then mixed at a fixed molar ratio to prepare the dopant solution. Enough dopant solution is then dropped onto the film and left on the substrate for the preset exposure time before starting the spin-coating for sufficient time to dry the film. To remove extra salts and dopants, an additional rinsing step is implemented by leaving enough solvent (ACN, ten times of the dopant solution as was adopted) on the sample before spinning it off. Either the exposure time or the dopant concentration can be varied to tune the doping levels. The exposure time was adjusted to produce PBTTT-TFSI⁻, PBTTT-TFSM⁻ at different doping levels with the concentration of the oxidizing agent fixed at $100 \times 10^{-3} \text{ mol L}^{-1}$. The concentration of dopant solution was controlled for PBTTT-TFO⁻ as the very fast migration of TFO⁻ into the bulk film makes it difficult to tune the doping levels of PBTTT-TFO⁻ through exposure time variation. For PBTTT-TFO⁻, the doping exposure time was fixed at 60 s for all the doped samples. For the FTIR samples shown in Figure 6, the electrolyte/dopant concentrations were varied as follows: at low doping regime (Figure 6a): $100/0.01 \times 10^{-3} \text{ mol L}^{-1}$ (BMP-OTF/PMA) for PBTTT-TFO⁻, $100/0.01 \times 10^{-3} \text{ mol L}^{-1}$ (BMP-TFSI/PMA) for PBTTT-TFSI⁻ and $100/0.03 \times 10^{-3} \text{ mol L}^{-1}$ (DMPI-TFSM/PMA) for PBTTT-TFSM⁻; at moderate doping regime (Figure 6b): $100/0.1 \times 10^{-3} \text{ mol L}^{-1}$ (BMP-OTF/PMA) for PBTTT-TFO⁻, $100/0.03 \times 10^{-3} \text{ mol L}^{-1}$ (BMP-TFSI/PMA) for PBTTT-TFSI⁻, $100/0.1 \times 10^{-3} \text{ mol L}^{-1}$ (DMPI-TFSM/PMA) for PBTTT-TFSM⁻ and $0.1 \times 10^{-3} \text{ mol L}^{-1}$ for FeCl₃. For the conductivities of PBTTT-TFSI⁻ shown in Figure 6c, three BMP-TFSI/PMA concentrations are selected in order as follows: $100/0.01 \times 10^{-3} \text{ mol L}^{-1}$, $100/0.03 \times 10^{-3} \text{ mol L}^{-1}$ and $100/0.1 \times 10^{-3} \text{ mol L}^{-1}$. A thin layer of Cytop when preparing the multifunctional devices to extend their lifetime was also spin-coated. The Cytop-M encapsulation layer with ≈500 nm thickness was spin-coated from a diluted Cytop solution (AGC Chemicals) with the cytop solvent (AGC Chemicals) at a fixed ratio of 1:2 (Cytop:solvent) at 2000 rpm for 60 s.

Two types of devices were employed in this work for conductivity-Seebeck and Hall effect measurements. The device fabrication procedures of Van der Pauw (VdP) devices and the multifunctional devices are shown in the Supporting Information Sections 1 and 7, respectively.

Characterization and Measurements: UV-vis spectra were measured by a Shimadzu UV-3600i dual beam spectrometer. FT-IR spectra were measured by a Bruker Vertex 70 V with a wide-band DLATGS detector in transmission geometry. GIWAXS data were collected at the 9A U-SAXS beam line at the Pohang Accelerator Laboratory, Pohang, Korea. Paracrystallinity was calculated as $g = \frac{1}{2\pi} \sqrt{\Delta_q d_{\pi-\pi}}$ where $d_{\pi-\pi}$ is the π -stacking distance and Δ_q is the FWHM of the π -stacking peak. Errors in g are dominated by the error in detector distance, resulting in a 0.2% error in measurements of g . All the room temperature conductivity data with the VdP devices are recorded on a manual probe station with an Agilent4155B semiconductor parameter analyzer (SPA) (see the Supporting Information Section 1 for the details). For the temperature dependence transport data, the measurements are performed with a multifunctional device in a Helium flow cryostat or a closed-loop Helium system (see the Supporting Information Section 8 for the details).

Simulation of Infrared Spectra of Polarons: The simulations were performed using the methodology described in refs. [28] and [29] further details can be found.^[45] Briefly, the Hamiltonian, parameterized for P3HT, includes hole hopping between thiophene units (with $t_h = -0.4 \text{ eV}$), the Coulomb attraction between holes and stationary anions, and hole-hole repulsion. Site disorder is also included—each cation (hole) thiophene unit is assigned a random Gaussian energy shift which represents, for example, the impact of an inhomogeneous electric field distribution. In the simulations in Figure 7, a Gaussian width of 0.2 eV (standard deviation) was taken. Chains containing 20 thiophene units with n dopant anions ($n = 1-4$) distributed in a zig-zag configuration about the chain center, as demonstrated in Figure 7a for a tetrapolaron complex ($n = 4$), were considered. An n -polaron complex consists of n stationary anions and n mobile holes. The spectrum, evaluated for each configuration of site disorder, is averaged over 2000 configurations to roughly match the width of the experimental spectra. Although parameterized for P3HT, PBTTT is similar enough in structure that the results will hold, at least qualitatively. Vibronic coupling was not included in the model since the basis set size became too large for tri- and tetrapolarons. The dielectric constant was set to unity to be consistent with the Ohno potential used to describe the Coulomb interaction between holes in a conjugated polymer chain.^[47]

Supporting Information

Supporting Information is available from the Wiley Online Library or from the author.

Acknowledgements

Financial support from the European Research Council for a Synergy grant SC2 (No. 610115) and from the Engineering and Physical Sciences Research Council (No. EP/R031894/1) is gratefully acknowledged. C.C. thanks the China Scholarship Council for financial support. H.S. acknowledges support from a Royal Society Research Professorship (RP\R1\201082), I.E.J. acknowledges funding through a Royal Society Newton International Fellowship. F.C.S. was supported by a grant from Department of Energy, DE-SC0020046. B.K. acknowledges the International Research & Development Program of the National Research Foundation of Korea (NRF) funded by the Ministry of Science and ICT (No. 2022K1A4A7A04094482).

Conflict of Interest

The authors declare no conflict of interest.

Data Availability Statement

The data that support the findings of this study are available from the corresponding author upon reasonable request.

Keywords

counterion effect, doping, organic electronics, semicrystalline polymers, thermoelectrics

Received: August 15, 2022

Revised: December 15, 2022

Published online: January 10, 2023

- [1] a) M. Dargusch, W.-D. Liu, Z.-G. Chen, *Adv. Sci.* **2020**, *7*, 2001362; b) S. Hong, Y. Gu, J. K. Seo, J. Wang, P. Liu, Y. S. Meng, S. Xu, R. Chen, *Sci. Adv.* **2019**, *5*, eaaw0536; c) K. Kang, T. Lee, *Nat. Nanotech.* **2018**, *13*, 97; d) J. Lee, H. Sul, Y. Jung, H. Kim, S. Han, J. Choi, J. Shin, D. Kim, J. Jung, S. Hong, S. H. Ko, *Adv. Funct. Mater.* **2020**, *30*, 2003328; e) C. Yu, Y. Li, X. Zhang, X. Huang, V. Malyarchuk, S. Wang, Y. Shi, L. Gao, Y. Su, Y. Zhang, H. Xu, R. T. Hanlon, Y. Huang, J. A. Rogers, *Proc. Natl. Acad. Sci. USA* **2014**, *111*, 12998; f) F. Zhang, Y. Zang, D. Huang, C. Di, D. Zhu, *Nat. Commun.* **2015**, *6*, 8356; g) W. Ren, Y. Sun, D. Zhao, A. Aili, S. Zhang, C. Shi, J. Zhang, H. Geng, J. Zhang, L. Zhang, J. Xiao, R. Yang, *Sci. Adv.* **2021**, *7*, eabe0586.
- [2] a) Q. Zhang, Y. Sun, W. Xu, D. Zhu, *Adv. Mater.* **2014**, *26*, 6829; b) Y. Wang, L. Yang, X.-L. Shi, X. Shi, L. Chen, M. S. Dargusch, J. Zou, Z.-G. Chen, *Adv. Mater.* **2019**, *31*, 1807916; c) H. Wang, C. Yu, *Joule* **2019**, *3*, 53; d) B. Russ, A. Glauddell, J. J. Urban, M. L. Chabiny, R. A. Segalman, *Nat. Rev. Mater.* **2016**, *1*, 16050; e) L. M. Cowen, J. Atoy, M. J. Carnie, D. Baran, B. C. Schroeder, *ECS J. Solid State Sci. Technol.* **2017**, *6*, N3080; f) M. Campoy-Quiles, *Philos. Trans. R. Soc., A* **2019**, *377*, 20180352.
- [3] C. Cho, K. L. Wallace, P. Tzeng, J.-H. Hsu, C. Yu, J. C. Grunlan, *Adv. Energy Mater.* **2016**, *6*, 1502168.
- [4] a) H. Wang, J.-H. Hsu, S.-I. Yi, S. L. Kim, K. Choi, G. Yang, C. Yu, *Adv. Mater.* **2015**, *27*, 6855; b) L. Wang, Z. Zhang, Y. Liu, B. Wang, L. Fang, J. Qiu, K. Zhang, S. Wang, *Nat. Commun.* **2018**, *9*, 3817.
- [5] L.-D. Zhao, S.-H. Lo, Y. Zhang, H. Sun, G. Tan, C. Uher, C. Wolverton, V. P. Dravid, M. G. Kanatzidis, *Nature* **2014**, *508*, 373.
- [6] I. Petsagkourakis, N. Kim, K. Tybrandt, I. Zozoulenko, X. Crispin, *Adv. Electron. Mater.* **2019**, *5*, 1800918.
- [7] a) J. He, T. M. Tritt, *Science* **2017**, *357*, eaak9997; b) G. J. Snyder, E. S. Toberer, *Nat. Mat.* **2008**, *7*, 105.
- [8] a) W. Zhao, J. Ding, Y. Zou, C.-A. Di, D. Zhu, *Chem. Soc. Rev.* **2020**, *49*, 7210; b) I. E. Jacobs, A. J. Moulé, *Adv. Mater.* **2017**, *29*, 1703063.
- [9] H. J. Goldsmid, in *Introduction to Thermoelectricity*, Vol. 121 (Ed: H. J. Goldsmid), Springer, Berlin **2010**, Ch. 3.
- [10] a) G. H. Kim, L. Shao, K. Zhang, K. P. Pipe, *Nat. Mater.* **2013**, *12*, 719; b) O. Bubnova, Z. U. Khan, A. Malti, S. Braun, M. Fahlman, M. Berggren, X. Crispin, *Nat. Mater.* **2011**, *10*, 429.
- [11] S. D. Kang, G. J. Snyder, *Nat. Mater.* **2017**, *16*, 252.
- [12] Y. Yamashita, J. Tsurumi, M. Ohno, R. Fujimoto, S. Kumagai, T. Kurosawa, T. Okamoto, J. Takeya, S. Watanabe, *Nature* **2019**, *572*, 634.
- [13] H. Tanaka, K. Kanahashi, N. Takekoshi, H. Mada, H. Ito, Y. Shimoi, H. Ohta, T. Takenobu, *Sci. Adv.* **2020**, *6*, eaay8065.
- [14] a) I. E. Jacobs, Y. Lin, Y. Huang, X. Ren, D. Simatos, C. Chen, D. Tjhe, M. Statz, L. Lai, P. A. Finn, W. G. Neal, G. D'Avino, V. Lemaury, S. Fratini, D. Beljonne, J. Strzalka, C. B. Nielsen, S. Barlow, S. R. Marder, I. McCulloch, H. Sirringhaus, *Adv. Mater.* **2022**, *34*, 2102988; b) I. E. Jacobs, G. D'Avino, V. Lemaury, Y. Lin, Y. Huang, C. Chen, T. F. Harrelson, W. Wood, L. J. Spalek, T. Mustafa, C. A. O'Keefe, X. Ren, D. Simatos, D. Tjhe, M. Statz, J. W. Strzalka, J.-K. Lee, I. McCulloch, S. Fratini, D. Beljonne, H. Sirringhaus, *J. Am. Chem. Soc.* **2022**, *144*, 3005.
- [15] a) H. Ito, H. Mada, K. Watanabe, H. Tanaka, T. Takenobu, *Commun. Phys.* **2021**, *4*, 8; b) Y. Lee, J. Park, J. Son, H. Y. Woo, J. Kwak, *Adv. Funct. Mater.* **2021**, *31*, 2006900.
- [16] O. Bubnova, Z. U. Khan, H. Wang, S. Braun, D. R. Evans, M. Fabretto, P. Hojati-Talemi, D. Dagnelund, J.-B. Arlin, Y. H. Geerts, S. Desbief, D. W. Breiby, J. W. Andreasen, R. Lazzaroni, W. M. Chen, I. Zozoulenko, M. Fahlman, P. J. Murphy, M. Berggren, X. Crispin, *Nat. Mater.* **2014**, *13*, 190.
- [17] Z. Liang, H. H. Choi, X. Luo, T. Liu, A. Abtahi, U. S. Ramasamy, J. A. Hitron, K. N. Baustert, J. L. Hempel, A. M. Boehm, A. Ansary, D. R. Strachan, J. Mei, C. Risko, V. Podzorov, K. R. Graham, *Nat. Mater.* **2021**, *20*, 518.
- [18] V. Vijayakumar, Y. Zhong, V. Untilova, M. Bahri, L. Herrmann, L. Biniek, N. Leclerc, M. Brinkmann, *Adv. Energy Mater.* **2019**, *9*, 1900266.
- [19] Y. Huang, D. H. Lukito Tjhe, I. E. Jacobs, X. Jiao, Q. He, M. Statz, X. Ren, X. Huang, I. McCulloch, M. Heeney, C. McNeill, H. Sirringhaus, *Appl. Phys. Lett.* **2021**, *119*, 111903.
- [20] a) K. Kang, S. Schott, D. Venkateshvaran, K. Broch, G. Schweicher, D. Harkin, C. Jellett, C. B. Nielsen, I. McCulloch, H. Sirringhaus, *Mater. Today Phys.* **2019**, *8*, 112; b) S. N. Patel, A. M. Glauddell, K. A. Peterson, E. M. Thomas, K. A. O'Hara, E. Lim, M. L. Chabiny, *Sci. Adv.* **2017**, *3*, e1700434.
- [21] a) M. L. Chabiny, M. F. Toney, R. J. Kline, I. McCulloch, M. Heeney, *J. Am. Chem. Soc.* **2007**, *129*, 3226; b) T. Schuettfort, B. Watts, L. Thomsen, M. Lee, H. Sirringhaus, C. R. McNeill, *ACS Nano* **2012**, *6*, 1849; c) I. McCulloch, M. Heeney, C. Bailey, K. Genevicius, I. MacDonald, M. Shkunov, D. Sparrowe, S. Tierney, R. Wagner, W. Zhang, M. L. Chabiny, R. J. Kline, M. D. McGehee, M. F. Toney, *Nat. Mater.* **2006**, *5*, 328; d) D. M. DeLongchamp, R. J. Kline, Y. Jung, D. S. Germack, E. K. Lin, A. J. Moad, L. J. Richter, M. F. Toney, M. Heeney, I. McCulloch, *ACS Nano* **2009**, *3*, 780.
- [22] D. Venkateshvaran, M. Nikolka, A. Sadhanala, V. Lemaury, M. Zelazny, M. Kepa, M. Hurhangee, A. J. Kronemeijer, V. Pecunia, I. Nasrallah, I. Romanov, K. Broch, I. McCulloch, D. Emin, Y. Olivier, J. Cornil, D. Beljonne, H. Sirringhaus, *Nature* **2014**, *515*, 384.
- [23] a) K. Kang, S. Watanabe, K. Broch, A. Sepe, A. Brown, I. Nasrallah, M. Nikolka, Z. Fei, M. Heeney, D. Matsumoto, K. Marumoto, H. Tanaka, S.-i. Kuroda, H. Sirringhaus, *Nat. Mater.* **2016**, *15*, 896; b) A. M. Glauddell, J. E. Cochran, S. N. Patel, M. L. Chabiny, *Adv. Energy Mater.* **2015**, *5*, 1401072.
- [24] a) V. I. Arkhipov, E. V. Emelianova, P. Heremans, H. Bässler, *Phys. Rev. B* **2005**, *72*, 235202; b) M. Koopmans, M. A. T. Leiviskä, J. Liu, J. Dong, L. Qiu, J. C. Hummelen, G. Portale, M. C. Heiber, L. J. A. Koster, *ACS Appl. Mater. Interfaces* **2020**, *12*, 56222; c) T. J. Aubry, J. C. Axtell, V. M. Basile, K. J. Winchell, J. R. Lindemuth, T. M. Porter, J.-Y. Liu, A. N. Alexandrova, C. P. Kubiak, S. H. Tolbert, A. M. Spokoyne, B. J. Schwartz, *Adv. Mater.* **2019**, *31*, 1805647.
- [25] E. M. Thomas, K. A. Peterson, A. H. Balzer, D. Rawlings, N. Stingelin, R. A. Segalman, M. L. Chabiny, *Adv. Electron. Mater.* **2020**, *6*, 2000595.
- [26] J. L. Bredas, G. B. Street, *Acc. Chem. Res.* **1985**, *18*, 309.
- [27] H. Tanaka, S. Nishio, H. Ito, S.-i. Kuroda, *Appl. Phys. Lett.* **2015**, *107*, 243302.
- [28] R. Ghosh, F. C. Spano, *Acc. Chem. Res.* **2020**, *53*, 2201.
- [29] M. B. Qarai, R. Ghosh, F. C. Spano, *J. Phys. Chem. C* **2021**, *125*, 24487.
- [30] S. Kasap, C. Koughia, H. E. Ruda, in *Springer Handbook of Electronic and Photonic Materials* (Eds: S. Kasap, P. Capper), Springer International Publishing, Cham, Switzerland **2017**, Ch. 2.
- [31] a) D. T. Scholes, P. Y. Yee, J. R. Lindemuth, H. Kang, J. Onorato, R. Ghosh, C. K. Luscombe, F. C. Spano, S. H. Tolbert, B. J. Schwartz, *Adv. Funct. Mater.* **2017**, *27*, 1702654; b) A. Abutaha, P. Kumar, E. Yildirim, W. Shi, S.-W. Yang, G. Wu, K. Hippalgaonkar, *Nat. Commun.* **2020**, *11*, 1737.
- [32] a) R. Noriega, J. Rivnay, K. Vandewal, F. P. V. Koch, N. Stingelin, P. Smith, M. F. Toney, A. Salleo, *Nat. Mater.* **2013**, *12*, 1038; b) J. Rivnay, R. Noriega, R. J. Kline, A. Salleo, M. F. Toney, *Phys. Rev. B* **2011**, *84*, 045203.
- [33] W. Liu, L. Müller, S. Ma, S. Barlow, S. R. Marder, W. Kowalsky, A. Köhn, R. Lovrincic, *J. Phys. Chem. C* **2018**, *122*, 27983.
- [34] a) X. Wang, X. Zhang, L. Sun, D. Lee, S. Lee, M. Wang, J. Zhao, Y. Shao-Horn, M. Dincă, T. Palacios, K. K. Gleason, *Sci. Adv.* **2018**, *4*, eaat5780; b) A. J. Heeger, N. S. Sariciftci, E. B. Namdas, in *Semiconducting and Metallic Polymers*, Oxford University Press, Oxford **2010**, Ch. 4; c) J. R. Reynolds, B. C. Thompson,

- T. A. Skotheim, in *Handbook of Conducting Polymers*, Vol. 2, (4th ed.), CRC Press, Boca Raton, FL **2019**, p. 15.
- [35] a) N. F. Mott, E. A. Davis, in *Electronic Processes in Non-Crystalline Materials*, Oxford University Press, Oxford **2012**, Ch. 6; b) O. Bubnova, X. Crispin, *Energy Environ. Sci.* **2012**, 5, 9345; c) S. Watanabe, M. Ohno, Y. Yamashita, T. Terashige, H. Okamoto, J. Takeya, *Phys. Rev. B* **2019**, 100, 241201.
- [36] A. Akrap, A. Ubaldini, E. Giannini, L. Forró, *Europhys. Lett.* **2014**, 107, 57008.
- [37] H. Overhof, P. Thomas, in *Insulating and Semiconducting Glasses*, Vol. 18 (Eds: H. Overhof, P. Thomas), World Scientific, Cincinnati, OH **2000**, Ch. 8.
- [38] M. Schwarze, C. Gaul, R. Scholz, F. Bussolotti, A. Hofacker, K. S. Schellhammer, B. Nell, B. D. Naab, Z. Bao, D. Spoltore, K. Vandewal, J. Widmer, S. Kera, N. Ueno, F. Ortmann, K. Leo, *Nat. Mater.* **2019**, 18, 242.
- [39] V. I. Arkhipov, P. Heremans, E. V. Emelianova, H. Bässler, *Phys. Rev. B* **2005**, 71, 045214.
- [40] C. G. Bischak, L. Q. Flagg, K. Yan, T. Rehman, D. W. Davies, R. J. Quezada, J. W. Onorato, C. K. Luscombe, Y. Diao, C.-Z. Li, D. S. Ginger, *J. Am. Chem. Soc.* **2020**, 142, 7434.
- [41] V. A. Kolesov, C. Fuentes-Hernandez, W.-F. Chou, N. Aizawa, F. A. Larrain, M. Wang, A. Perrotta, S. Choi, S. Graham, G. C. Bazan, T.-Q. Nguyen, S. R. Marder, B. Kippelen, *Nat. Mater.* **2017**, 16, 474.
- [42] R. Ghosh, A. R. Chew, J. Onorato, V. Pakhnyuk, C. K. Luscombe, A. Salleo, F. C. Spano, *J. Phys. Chem. C* **2018**, 122, 18048.
- [43] J. O. Guardado, A. Salleo, *Adv. Funct. Mater.* **2017**, 27, 1701791.
- [44] D. Rawlings, E. M. Thomas, R. A. Segalman, M. L. Chabinyk, *Chem. Anal. Biol. Fate: Polynucl. Aromat. Hydrocarbons, Int. Symp., 5th* **2019**, 31, 8820.
- [45] M. B. Qarai, R. Ghosh, F. C. Spano, unpublished.
- [46] C. Enengl, S. Enengl, S. Pluczyk, M. Havlicek, M. Lapkowski, H. Neugebauer, E. Ehrenfreund, *ChemPhysChem* **2016**, 17, 3836.
- [47] a) K. Ohno, *Theor. Chim. Acta* **1964**, 2, 219; b) I. R. Ducasse, T. E. Miller, Z. G. Soos, *J. Chem. Phys.* **1982**, 76, 4094.